Analytical Properties of Time-of-Flight PET Data

Sanghee Cho, **Sangtae Ahn**, **Quanzheng Li**, and **Richard M. Leahy**

Signal and Image Processing Institute, University of Southern California, Los Angeles, CA 90089, USA

Richard M. Leahy: leahy@sipi.usc.edu

Abstract

We investigate the analytical properties of time-of-flight (TOF) positron emission tomography (PET) sinograms, where the data are modeled as line integrals weighted by a spatially invariant TOF kernel. First, we investigate the Fourier transform properties of 2D TOF data and extend the "bow-tie" property of the 2D Radon transform to the time of flight case. Second, we describe a new exact Fourier rebinning method, TOF-FOREX, based on the Fourier transform in the time-of-flight variable. We then combine TOF-FOREX rebinning with a direct extension of the projection slice theorem to TOF data, to perform fast 3D TOF PET image reconstruction. Finally, we illustrate these properties using simulated data.

1. Introduction

It has long been known that time-of-flight (TOF) information can be used to improve image quality in PET. While TOF systems were first developed more than 20 years ago (Mullani et al. 1981, Ter-Pogossian et al. 1982, Gariod et al. 1982), the detectors available at that time did not have the combination of speed, stopping power and light output necessary for a practical clinical system. The recent development of fast scintillators, such as LSO (Melcher and Schweitzer 1992, Moses and Derenzo 1999, Moszynski et al. 2006) and LaBr3 (Kuhn et al. 2004, Surti et al. 2006), now makes such systems practical.

The TOF measurement is the difference between the arrival times at the detectors of two photons produced by a single annihilation event. High resolution measurement of this time difference would allow one to determine the precise location at which the annihilation occurred. In practice, limited timing resolution results in an uncertainty in this location, typically characterized by a convolution kernel which is used to weight the line integral along the line of response (LOR) when modeling TOF sinograms. Even with this uncertainty, TOF data increases SNR at matched image resolution compared to data without timing information (Tomitani 1981, Moses 2003, Harrison et al. 2004). The uncertainty in the TOF measurement is typically modeled as a Gaussian distribution and assumed to be shift invariant along the LOR (Mallon and Grangeat 1992, Defrise et al. 2005). Based on this model, images have been reconstructed from TOF data, both analytically (Tomitani 1981, Mallon and Grangeat 1992, Conti et al. 2005, Watson 2007) and iteratively (Snyder and Politte 1983, Chen and Metz 1985, Parra and Barrett 1998, Conti et al. 2005).

In this paper we derive two analytical properties of TOF PET sinograms that follow from taking a Fourier transform in the TOF variable. First, we examine the frequency response of

2D TOF PET sinograms and extend the "bow-tie" property of the standard 2D sinogram (Rattey and Lindgren 1981) to the TOF case. By analyzing the impulse response, as in (Rattey and Lindgren 1981), we show that the 3D Fourier transform of the TOF sinogram of a 2D image has a modified bow-tie property. This property could be used for reduction of noise or scatter components in the data, or for sinogram restoration for limited angle tomography (Karp et al. 1988).

We then derive an exact mapping between fully 3D TOF PET and stacked 2D TOF PET sinograms, again using the Fourier transform properties of the TOF data. This mapping can be regarded as an extension to TOF of FOREX, the exact Fourier rebinning equations for standard sinograms in (Defrise et al. 1997, Liu et al. 1999). This result differs from the recent TOF rebinning methods in (Defrise et al. 2005) and (Vandenberghe et al. 2006). The latter is an approximate method that operates in the native coordinates of the TOF sinograms while that in (Defrise et al. 2005) uses Fourier transform relationships and the stationary phase approximation. Defrise *et al* (2005) also describe two exact rebinning methods, both based on consistency conditions and requiring the calculation of partial derivatives. The result described here uses a Fourier transform in the TOF variable to derive an exact relationship. While this avoids the need for calculation of partial derivatives, it does involve the estimation of missing data, similarly to the original FOREX rebinning method for standard sinograms (Defrise et al. 1997, Liu et al. 1999). We note that this issue does not arise for inverse rebinning, i.e. computing oblique sinograms from the stacked 2D sinograms, a property that we made use of in developing fast forward and backprojection operators for use in iterative image reconstruction (Cho et al. 2007).

To illustrate this result, we combine the rebinning operator with a direct 2D Fourier reconstruction method for 3D TOF PET. The Fourier reconstruction method uses TOF form of the projection slice theorem that follows from the development of the bow tie property. Simulations illustrating the bow-tie property, Fourier rebinning and direct Fourier reconstruction conclude the paper.

2. The Time of Flight Model

Following Defrise *et al* (2005), we represent the 3D TOF PET data p_{3D} for a cylindrical scanner geometry, illustrated in figure 1, as a line integral weighted by the TOF kernel h:

$$p_{3D}(s,\phi,z,\delta;t) = \sqrt{1+\delta^2} \int_{-\infty}^{\infty} f(s\cos\phi - l\sin\phi, s\sin\phi + l\cos\phi, z+l\delta)h(t - l\sqrt{1+\delta^2})dl \quad (1)$$

where f represents the 3D object, s and φ are the radial and angular coordinates, respectively, z is the axial midpoint of each LOR, δ is the tangent of the oblique angle θ, and t is the TOF variable. The TOF kernel h, often modeled as a Gaussian function (Conti et al. 2005), is assumed to be shift invariant, so that the integral in (1) is in the form of a convolution.

As a special case, we can write the stacked 2D TOF direct sinograms p_{2D} by setting the tangent δ of the oblique angle to zero in (1) as follows:

$$p_{2D}(s,\phi,z;t)=p_{3D}(s,\phi,z,\delta=0;t)=\int_{-\infty}^{\infty}f(s\cos\phi-l\sin\phi,s\sin\phi+l\cos\phi,z)h(t-l)dl. \quad (2)$$

The absence of time of flight information is equivalent to setting $h=1$ in which case p_{3D} in (1) reduces to the 3D non-TOF data p_{3D}^{nonTOF}:

$$p_{3D}^{\mathrm{nonTOF}}(s,\phi,z,\delta)=\sqrt{1+\delta^2}\int_{-\infty}^{\infty}f(s\cos\phi-l\sin\phi,s\sin\phi+l\cos\phi,z+l\delta)dl. \quad (3)$$

Taking the 1D Fourier transform of the 3D TOF PET data p_{3D} in (1) with respect to the TOF variable t, we have:

$$
\begin{aligned}
&P_{3D}(s,\phi,z,\delta;\omega_t)\\
&=\int_{-\infty}^{\infty}p_{3D}(s,\phi,z,\delta;t)e^{-i\omega_t t}dt\\
&=\sqrt{1+\delta^2}H(\omega_t)\int_{-\infty}^{\infty}f(s\cos\phi-l\sin\phi,s\sin\phi+l\cos\phi,z+l\delta)e^{-i\omega_t l\sqrt{1+\delta^2}}dl
\end{aligned}
\quad (4)
$$

where ω_t is the frequency variable corresponding to t and H is the 1D FT of h. A stacked 2D version of the above equation, that is, the 1D Fourier transform of p_{2D} in (2) with respect to t, is given by

$$P_{2D}(s,\phi,z;\omega_t)=H(\omega_t)\int_{-\infty}^{\infty}f(s\cos\phi-l\sin\phi,s\sin\phi+l\cos\phi,z)e^{-i\omega_t l}dl. \quad (5)$$

The Fourier transform with respect to the TOF variable t takes the TOF kernel term H out of the integrals in (4) and (5) so P_{3D} in (4) is similar to the non-TOF p_{3D}^{nonTOF} in (3) except for the scaling factor $H(\omega_t)$ and the phase modulation term $\exp(-i\omega_t l\sqrt{1+\delta^2})$. It is this similarity of the non-TOF data p_{3D}^{nonTOF} and the Fourier transform P_{3D} of the TOF data p_{3D}, with respect to t, that enables us to extend the properties of non-TOF data to the TOF case. This is the observation that underlies this paper, and from it we derive the bow-tie property for 2D TOF data, a projection slice theorem for 2D TOF data, and exact rebinning mappings for the 3D and the stacked 2D TOF data.

3. Analytical properties of TOF PET data

3.1. 2D TOF PET data

3.1.1. Bow-tie property—Rattey and Lindgren (1981) showed that the 2D Fourier transform of a 2D non-TOF PET sinogram has almost all of its energy confined to a characteristic bowtie shaped region, where the size of the bow-tie is determined by the radius of the object. This result followed directly from considering the Fourier transform of the sinogram of a point source. Here we extend this analysis to the TOF case.

Consider $P_{2D}(s,\varphi,z,\omega_t)$, the stacked 2D TOF sinograms after taking the Fourier transform in t. Since we focus here on a property of the 2D sinogram, we omit the z variable in the

following. First, we take the 1D Fourier transform of $P_{2D}(s, \varphi; \omega_t)$ with respect to s for the case where the object is a 2D impulse at (x_0, y_0), $f(x, y) = \delta_2(x - x_0, y - y_0)$:

$$\tilde{\wp}_{2D}(\omega_s, \phi; \omega_t) = \int_{-\infty}^{\infty} P_{2D}(s, \phi; \omega_t) e^{-i\omega_s s} ds \quad (6)$$

$$= H(\omega_t) \int_{-\infty}^{\infty} \int_{-\infty}^{\infty} f(x, y) e^{-i(\omega_t(y\cos\phi - x\sin\phi) + \omega_s(x\cos\phi + y\sin\phi))} dx dy \quad (7)$$

$$= H(\omega_t) \int_{-\infty}^{\infty} \int_{-\infty}^{\infty} \delta_2(x - x_0, y - y_0) e^{-i(\omega_t(y\cos\phi - x\sin\phi) + \omega_s(x\cos\phi + y\sin\phi))} dx dy \quad (8)$$

$$= H(\omega_t) e^{-ir_0 \sqrt{\omega_t^2 + \omega_s^2} \cos(\phi - \phi_0 + \phi_1)} \quad (9)$$

where $r_0 = \sqrt{x_0^2 + y_0^2}$, $\varphi_0 = \arctan(y_0/x_0)$, $\varphi_1 = \arctan(\omega_t/\omega_s)$. We make the change of variable $s\cos\varphi - l\sin\varphi = x$ and $s\sin\varphi + l\cos\varphi = y$ in (7). Next we take the 1D Fourier transform of $\wp_{2D}(\omega_s, \varphi; \omega_t)$ with respect to φ:

$$\wp_{2D}(\omega_s, \omega_\phi; \omega_t) = \int_{-\infty}^{\infty} \tilde{\wp}_{2D}(\omega_s, \phi; \omega_t) e^{-i\omega_\phi \phi} d\phi \quad (10)$$

$$= H(\omega_t) \int_{-\infty}^{\infty} e^{-ir_0 \sqrt{\omega_s^2 + \omega_t^2} \cos(\phi - \phi_0 + \phi_1)} e^{-i\omega_\phi \phi} d\phi. \quad (11)$$

We note that since $\tilde{\wp}_{2D}$ is a 2π periodic function in φ, it can be directly represented through its Fourier series. However, here we follow the notation of (Rattey and Lindgren 1981) and use the generalized Fourier transform of the periodic function in (11), which results in the weighted impulse train in ω_φ:

$$\wp_{2D}(\omega_s, \omega_\phi; \omega_t) = H(\omega_t) \sum_{m=-\infty}^{\infty} \left(2\pi e^{-im(\pi/2 + \phi_0')} J_m \left(r_0 \sqrt{\omega_s^2 + \omega_t^2} \right) \right) \delta(\omega_\phi - m) \quad (12)$$

where $\phi_0' = \phi_0 - \phi_1$ and J_m is the mth order Bessel function of the first kind:

$$J_m(r) = \frac{1}{2\pi} \int_{-\pi}^{\pi} e^{i(m\phi - r\sin\phi)} d\phi.$$

As observed by Rattey and Lindgren (1981) for the non TOF case (equivalent to $\omega_t = 0$ in (12)), the properties of the Bessel function are such that $\wp_{2D}(\omega_s, \omega_\varphi; \omega_t)$ in (12) is

approximately zero for $|\omega_\phi| > r_0 \sqrt{\omega_s^2 + \omega_t^2} + 1$ and the energy of the function is approximately contained within the region

$$\mathscr{B}(\omega_t) = \left\{ (\omega_s, \omega_\phi) : |\omega_\phi| \le \left| r_0 \sqrt{\omega_s^2 + \omega_t^2} \right| + 1 \right\} \quad (13)$$

This region is bounded by a hyperbolic curve in the $(\omega_s, \omega_\varphi)$ plane for $\omega_t > 0$. When $\omega_t = 0$, $\mathscr{B}$ becomes the well known bow-tie region for non-TOF data (Rattey and Lindgren 1981). Examples that illustrate this property are shown in Section 4

3.1.2. Projection slice theorem for 2D TOF PET—One can also derive a projection slice theorem for 2D TOF data using (7) as follows:

$$\tilde{\wp}_{2D}(\omega_s, \phi; \omega_t) = H(\omega_t) \int_{-\infty}^{\infty} \int_{-\infty}^{\infty} f(x, y) e^{-i((\omega_s \cos\phi - \omega_t \sin\phi)x + (\omega_s \sin\phi + \omega_t \cos\phi)y)} dx dy \quad (14)$$

$$= H(\omega_t) F(\omega_s \cos\phi - \omega_t \sin\phi, \omega_s \sin\phi + \omega_t \cos\phi) \quad (15)$$

where F is the 2D Fourier transform of the object f. We can use (15) to directly compute the 2D image Fourier transform for 2D TOF data for each value of ω_t. Equivalent projection slice theorems for TOF-PET have previously been shown in (Snyder et al. 1981, Tomitani 1981, Watson 2007). We use this theorem in Section 4 to perform fully 3D reconstruction through a combination of Fourier rebinning, as described in the next section, and a stacked 2D direct Fourier reconstruction method.

3.2. Exact rebinning mappings between 3D and stacked 2D TOF PET sinograms: TOF-FOREX

Here we derive an exact mapping between 3D TOF sinograms and stacked 2D TOF direct sinograms using Fourier transform relationships. The exact mapping can be used for either exact rebinning or inverse rebinning as in (Liu et al. 1999) and (Cho et al. 2007) for non-TOF data.

3.2.1. An exact inverse rebinning mapping—We take the 2D Fourier transform of $P_{3D}(s, \varphi, z, \delta; \omega_t)$ in (4) with respect to s and z as follows:

$$\wp_{3D}(\omega_s, \phi, \omega_z, \delta; \omega_t) = \int_{-\infty}^{\infty} \int_{-\infty}^{\infty} P_{3D}(s, \phi, z, \delta; \omega_t) e^{-i(\omega_s s + \omega_z z)} ds dz = \sqrt{1+\delta^2} H(\omega_t) \tilde{\wp}_{3D}(\omega_s, \phi, \omega_z, \delta; \omega_t) \quad (16)$$

where

$$\tilde{\wp}_{3D}(\omega_s, \phi, \omega_z, \delta; \omega_t) = \int_{-\infty}^{\infty} \int_{-\infty}^{\infty} \int_{-\infty}^{\infty} f(s \cos\phi - l \sin\phi, s \sin\phi + l \cos\phi, z + l\delta) \cdot e^{-i\omega_t l \sqrt{1+\delta^2}} dl e^{-j(\omega_s s + \omega_z z)} ds dz \quad (17)$$

$$= \int_{-\infty}^{\infty} \int_{-\infty}^{\infty} F_z(x, y, \omega_z) e^{-ix(\omega_s \cos\phi - (\omega_t \sqrt{1+\delta^2} - \delta\omega_z)\sin\phi)} \cdot e^{-iy(\omega_s \sin\phi + (\omega_t \sqrt{1+\delta^2} - \delta\omega_z)\cos\phi)} dx dy \quad (18)$$

$$= F_{3D}(\tilde{\omega}_x, \tilde{\omega}_y, \omega_z). \quad (19)$$

where $\tilde{\omega}_x = \omega_s \cos\phi - (\omega_t \sqrt{1+\delta^2} - \delta\omega_z)\sin\phi$, $\tilde{\omega}_y = \omega_s \sin\phi + (\omega_t \sqrt{1+\delta^2} - \delta\omega_z)\cos\phi$, F_{3D} is the 3D Fourier transform of f, and $F_z(x, y, \omega_z)$ in (18) is the 1D Fourier transform of $f(x, y, z)$ with respect to z. The change of variable, $s \cos\varphi - l \sin\varphi = x$ and $s \sin\varphi + l \cos\varphi = y$, and the shifting property of Fourier transform are used to obtain (18). One can view (19) as an extension of (15) to 3D TOF PET data, which is equivalent to (3) in (Watson 2007), although here the result is derived directly in terms of the parametrization used for data collected in a cylindrical scanner.

Similarly, we take the 2D Fourier transform of $P_{2D}(s, \varphi, z, \omega_t)$ in (5) with respect to s and z:

$$\wp_{2D}(\omega_s', \phi', \omega_z'; \omega_t') = \int_{-\infty}^{\infty}\int_{-\infty}^{\infty} P_{2D}(s, \phi', z; \omega_t')e^{-i(\omega_s' s + \omega_z' z)}dsdz = H(\omega_t')\tilde{\wp}_{2D}(\omega_s', \phi', \omega_z'; \omega_t') \quad (20)$$

where

$$\tilde{\wp}_{2D}(\omega_s', \phi', \omega_z'; \omega_t') = \int_{-\infty}^{\infty}\int_{-\infty}^{\infty} F_z(x, y, \omega_z')e^{-i(x(\omega_s'\cos\phi' - \omega_t'\sin\phi') + y(\omega_s'\sin\phi' + \omega_t'\cos\phi'))}dxdy \quad (21)$$

$$= F_{3D}(\tilde{\omega}_x', \tilde{\omega}_y', \omega_z) \quad (22)$$

which can be obtained directly from (18) by setting δ to zero. Where $\tilde{\omega}_x' = \omega_s'\cos\phi' - \omega_t'\sin\phi'$ and $\tilde{\omega}_y' = \omega_s'\sin\phi' + \omega_t'\cos\phi'$ in (22), and the primed notations, ω_s', φ', ω_z', and ω_t', are used to distinguish the arguments of $\wp_{2D}$ and $\tilde{\wp}_{2D}$ from those of $\wp_{3D}$ and $\tilde{\wp}_{3D}$.

Comparing (18) and (21), or (19) and (22), we see that

$\tilde{\wp}_{3D}(\omega_s, \phi, \omega_z, \delta; \omega_t) = \tilde{\wp}_{2D}(\omega_s', \phi', \omega_z'; \omega_t')$ provided the following conditions are satisfied

$$\omega_s'\cos\phi' - \omega_t'\sin\phi' = \omega_s\cos\phi - (\omega_t\sqrt{1+\delta^2} - \delta\omega_z)\sin\phi \quad (23)$$

$$\omega_s'\sin\phi' + \omega_t'\cos\phi' = \omega_s\sin\phi + (\omega_t\sqrt{1+\delta^2} - \delta\omega_z)\cos\phi \quad (24)$$

$$\omega_z' = \omega_z. \quad (25)$$

We can rewrite (23) and (24) as follows:

$$\sqrt{\omega_s'^2 + \omega_t'^2}\cos(\phi' + \alpha') = \sqrt{\omega_s^2 + \chi^2}\cos(\phi + \beta) \quad (26)$$

$$\sqrt{\omega_s'^2 + \omega_t'^2}\sin(\phi' + \alpha') = \sqrt{\omega_s^2 + \chi^2}\sin(\phi + \beta) \quad (27)$$

where

$$\chi = \omega_t \sqrt{1+\delta^2} - \delta\omega_z, \alpha' = \arctan(\omega_t'/\omega_s'), \beta = \arctan(\chi/\omega_s).$$

To complete the development we need to find a transformation between $\{\omega_s', \phi', \omega_z', \omega_t'\}$ and $\{\omega_s, \phi, \omega_z, \omega_t\}$ that satisfies (25)–(27). We note that there is more than one transformation that satisfies these three equations. We first select a transformation suitable for inverse rebinning and then address the problem of rebinning from 3D to stacked 2D data.

The following transformation satisfies (25)–(27):

$$\omega_s' = \omega_s \sqrt{1+(\chi/\omega_s)^2}, \phi' = \phi+\beta, \omega_z' = \omega_z, \omega_t' = 0. \quad (28)$$

Substituting these transformations into (20) and equating to (16) we obtain the final form of the inverse rebinning relationship:

$$\wp_{3D}(\omega_s, \phi, \omega_z, \delta; \omega_t) = \sqrt{1+\delta^2}(H(\omega_t)/H(0))\wp_{2D}\left(\omega_s\sqrt{1+(\chi/\omega_s)^2}, \phi+\beta, \omega_z; 0\right). \quad (29)$$

Note that this inverse rebinning mapping use only the stacked 2D TOF data for $\omega_t = 0$ which is equivalent to the non-TOF data.

3.2.2. An exact rebinning mapping—The inverse rebinning result (28) could also be used to rebin the data. However this would rebin the 3D TOF sinograms into stacked 2D non-TOF sinograms and hence lose the benefits of the TOF information. Whether and how such loss of TOF information would affect the reconstruction image quality is not known at this time. In this paper we consider an alternative mapping that retains the TOF information while still satisfying (25)–(27):

$$\omega_s' = \omega_s\sqrt{1+(\chi^2-\omega_t^2)/\omega_s^2}, \phi' = \phi+\beta-\alpha', \omega_z' = \omega_z, \omega_t' = \omega_t. \quad (30)$$

Note that this mapping is defined only for $\omega_t^2 \leq \omega_s^2 + \chi^2$. Using the inverse of the transformation in (30), we obtain the following exact rebinning equation:

$$\wp_{2D}(\omega_s', \phi', \omega_z'; \omega_t') = \frac{1}{\sqrt{1+\delta^2}}\wp_{3D}(\tilde{\omega}_s', \phi'+\alpha'-\beta', \omega_z', \delta; \omega_t') \quad (31)$$

where

$$\chi' = \omega_t'\sqrt{1+\delta^2} - \delta\omega_z', \tilde{\omega}_s' = \omega_s'\sqrt{1+(\omega_t'^2-\chi'^2)/\omega_s'^2}, \beta' = \arctan(\chi'/\tilde{\omega}_s').$$

To implement an exact rebinning mapping, we first perform inverse rebinning to estimate the missing oblique TOF sinograms that are required to compute the Fourier transform in z. We do this using the direct plane sinogram data. A normalization step is required to account for the variable contribution to each frequency bin in $\wp_{2D}(\omega_s', \phi', \omega_z'; \omega_t')$ from the oblique sinogram in $\wp_{3D}$ (Liu et al. 1999). After the 3D TOF sinogram is rebinned to stacked 2D

direct TOF sinograms, any 2D TOF image reconstruction method can be applied to each 2D direct TOF sinogram. In the results shown below we use a 2D direct Fourier reconstruction method that makes use of the TOF projection slice theorem (15).

The exact inverse rebinning equation (29) and the exact rebinning equation (31) reduce to the exact rebinning equations used in FOREX (Liu et al. 1999) when $\omega_t' = \omega_t = 0$. We therefore refer to the rebinning methods in (29) and (31) as TOF-FOREX.

4. Results

4.1. Simulation setup

We performed simulation studies to illustrate the analytical results derived in the previous section. We simulated a 3D TOF cylindrical PET system whose parameters are shown in Table 1. A 3D TOF projector was implemented using Siddon's ray tracing algorithm (Siddon 1985) with a TOF kernel weight as in (Groiselle and Glick 2004). A Gaussian function was used for the TOF kernel. Two different TOF resolutions, 500 and 250 ps, were tested. These values were used for both the full width at half maximum (FWHM) of the TOF kernel and for the TOF bin interval, leading to 7 and 15 TOF bins, respectively over the field of view. A scaled version of the 3D Hoffman digital brain phantom was used as an object for data generation. The phantom was scaled since the benefits of TOF information are larger for larger objects. Here, the scaled phantom size was 512mm×512mm×164mm, and we note that one would not expect to see such large improvements from TOF data in human brain studies.

Figure 2 shows examples of TOF data for a direct plane ($\delta = 0$). Figures 2(a) and (b) show the raw TOF data p_{3D} in (1) for different values of the TOF variable t. Figures 2(c) and (d) show the magnitude of the TOF data after taking the 1-D Fourier transform in t, as defined in (4), for different values of ω_t. Note that P_{3D} for $\omega_t = 0$, shown in Figure 2(c), is equivalent to the non-TOF data.

4.2. Aliasing in the TOF bin direction

Taking the Fourier transform with respect to the TOF variable may cause aliasing since the sampling frequency in the TOF variable is low. However, the bandwidth along the LOR is limited through convolution with the TOF kernel which limits the effects of aliasing. We quantified aliasing errors for the Hoffman brain phantom in the PET system with the parameters in Table 1. The fraction of the total signal power that was aliased (that is, appearing in the wrong frequency location as a result of undersampling) was less than 1% of the total for both the 250 and 500 ps timing resolutions.

4.3. Bow-tie property

Figure 3 shows examples of the magnitude of the Fourier transform $\wp_{2D}(\omega_s, \omega_\varphi; \omega_t)$ of $\wp_{2D}(s, \varphi; \omega_t)$ for a direct plane ($\delta = 0$) at 250 ps TOF resolution. Each block in the figure shows the magnitude for a different frequency index in ω_t. As ω_t increases, the separation between the two branches of the hyperbola increases. The solid hyperbolic curve in figure 3(d) shows the boundaries of the bow-tie region calculated from the relationship in (13).

Note that the calculated values of $\wp_{2D}(\omega_s, \omega_\varphi; \omega_t)$ are indeed largely contained in these hyperbolically confined regions.

4.4. 3D TOF PET image reconstruction using exact Fourier rebinning (TOF-FOREX)

To investigate a practical implementation of the exact rebinning algorithm, TOF-FOREX, we generated noiseless 3D TOF sinograms and rebinned using the exact rebinning described in Section 3. We then compared the rebinned stacked 2D TOF sinograms with those directly calculated from the phantom image as shown in Figure 4. The rebinned values agree closely with the directly calculated values. The normalized root-mean-squared (RMS) error between the two 2D direct sinograms was less than 6% for both 500 and 250 ps timing resolutions. The differences are probably caused by interpolation errors when rebinning the digitized data compared to direct calculation, and the impact of the small degree of aliasing reported above.

Next we generated noisy 3D TOF sinograms based on a total of 200 million counts for TOF timing resolutions of 500 and 250 ps. Figure 5 shows the SNR improvement resulting from rebinning of all oblique data into a set of stacked 2D sinograms.

After rebinning, we reconstructed 2D images from the noisy rebinned data using 2D direct Fourier reconstruction based on (15). We used a gridding method for 2D interpolation based on a Kaiser-Bessel convolution kernel (Jackson et al. 1991) to obtain frequency samples in the Cartesian grid before taking the 2D inverse Fourier transform to reconstruct each slice. For comparison, a 3D non-TOF sinogram with the same total number of counts was also generated and FOREX applied. We compared the reconstructed images at the axial center plane in Figure 6. As expected, we see the SNR gains resulting from the use of TOF data compared to non-TOF data with a matched number of counts, and further improvements when increasing timing resolution from 500 to 250 ps.

5. Conclusions

The main idea in this paper was to explore the properties of TOF data by taking the 1D Fourier transform in the TOF variable *t*. We see that in this case, the resulting sinograms share similar properties to that of the non-TOF sinograms; this is not the case when dealing directly with TOF data. We then explored the 2D Fourier transform properties, with respect to (*s*, φ), and showed how the bow-tie property extends to TOF data. We also were able to use the Fourier properties of TOF data to derive an exact rebinning method for 3D TOF data.

Clearly, current TOF timing resolution limits the corresponding spatial resolution along the LOR in the time of flight variable. While we were concerned that this would limit our ability to use Fourier transforms in *t*, in practice the bandlimiting effect of the TOF kernel appears to ameliorate potential aliasing effects. This appears to be the case even at currently achievable timing resolutions of 500 ps (Conti et al. 2005, Surti et al. 2006, Surti et al. 2007).

Although TOF-FOREX is exact, it requires more computation compared to the approximated TOF-FORE in (Defrise et al. 2005) due to the inverse rebinning step required

to estimate missing planes. Consequently it is not clear that the exact rebinning operator will be of direct practical value, although further investigation in this direction is planned.

Another application of the result presented here would be to use the inverse rebinning equation (29) to design a fully 3D TOF PET projector for iterative reconstruction as an extension of our recent fast maximum a posteriori (MAP) method (Cho et al. 2007) as an alternative to other iterative TOF reconstruction methods for binned (Matej et al. 2006), or list mode (Snyder and Politte 1983, Groiselle and Glick 2004, Surti et al. 2007) data.
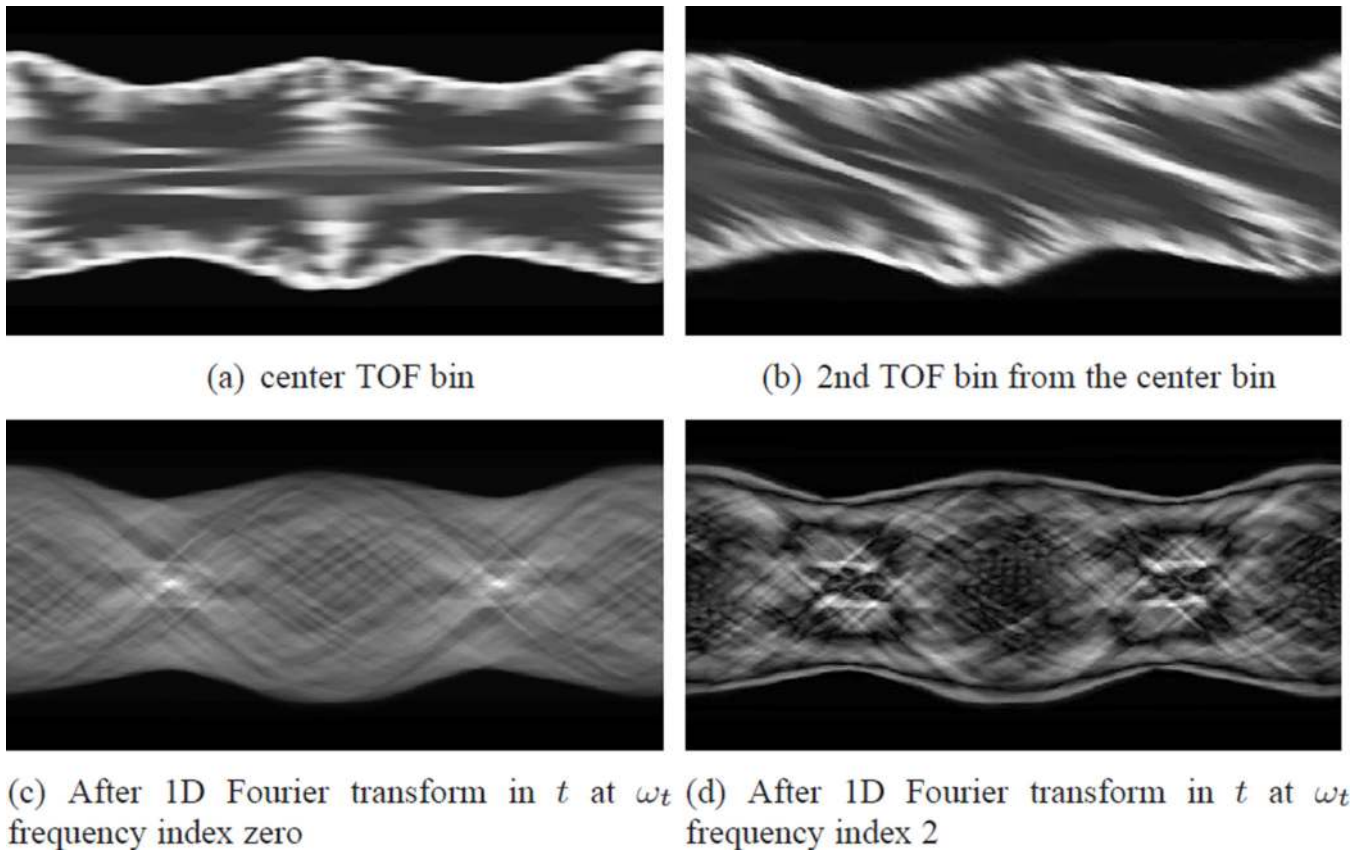
References

Chen CT, Metz CE. A simplified EM reconstruction for TOFPET. IEEE Trans. Nucl. Sci. 1985; 32(1): 885–888.

Cho S, Li Q, Ahn S, Bai B, Leahy RM. Iterative image reconstruction using inverse Fourier rebinning for fully 3-D PET. IEEE Trans. Med. Imag. 2007; 26(5):745–756.

Conti M, Bendrien B, Casey M, Chen M, Kehren F, Michel C, Panin V. First experimental results of time-of-flight reconstruction on an LSO PET scanner. Phys. Med. Biol. 2005; 50:4507–4526. [PubMed: 16177486]

Defrise M, Casey ME, Michel C, Conti M. Fourier rebinning of time-of-flight PET data. Phys. Med. Biol. 2005; 50:2749–2763. [PubMed: 15930600]

Defrise M, Kinahan PE, Townsend DW, Michel C, Sibomana M, Newport DF. Exact and approximate rebinning algorithms for 3-D PET data. IEEE Trans. Med. Imag. 1997; 16(2):145–158.

Gariod, R.; Allemand, R.; Cormoreche, E.; Laval, M.; Moszynski, M. Proc. IEEE Workshop on Time-of-Flight Emission Tomography. Louis, MO: Washington University, St; 1982. The 'LETI' positron tomograph architecture and time of flight improvements; p. 25-29.

Groiselle CJ, Glick SJ. 3D PET list-mode iterative reconstruction using time-of-flight information. Proc. IEEE Nuclear Science Symp. Medical Imaging Conf. 2004:2633–2638.

Harrison RL, Alessio AM, Kinahan PE, Lewellen TK. Signal to noise ratio in simulations of time-of-flight positron emission tomography. Proc. IEEE Nuclear Science Symp. Medical Imaging Conf. 2004:4080–4083.

Jackson JI, Meyer CH, Nishimura DG, Macovski A. Selection of a convolution function for Fourier inversion using gridding. IEEE Trans. Med. Imag. 1991; 10(3):473–478.

Karp JS, Muehllehner G, Lewitt RM. Constrained Fourier space method for compensation of missing data in emission computed tomography. IEEE Trans. Med. Imag. 1988; 7(1):21–25.

Kuhn A, Surti S, Karp J, Raby P, Shah K, Perkins A, Muehllehner G. Design of a lanthanum bromide detector for time-of-flight PET. IEEE Trans. Nucl. Sci. 2004; 51:2550–2557.

Liu X, Defrise M, Michel C, Sibomana M, Comtat C, Kinahan P, Townsend D. Exact rebinning methods for three-dimensional PET. IEEE Trans. Med. Imag. 1999; 18(8):657–664.

Mallon A, Grangeat P. Three-dimensional PET reconstruction with time-of-flight measurement. Phys. Med. Biol. 1992; 37:717–729. [PubMed: 1565699]

Matej S, Jayanthi S, Surti S, Daube-Witherspoon ME, Muehllenhner G, Karp JS. Efficient 3D TOF PET reconstruction using view-grouped histo-images: DIRECT - Direct Image Reconstruction for TOF. Proc. IEEE Nuclear Science Symp. Medical Imaging Conf. 2006:1728–1735.

Melcher CL, Schweitzer JS. Cerium-doped lutetium oxyorthosilicate: a fast, efficient new scintillator. IEEE Trans. Nucl. Sci. 1992; 39:502–505.

Moses WW. Time of flight in PET revisited. IEEE Trans. Nucl. Sci. 2003; 50:1325–1330.

Moses WW, Derenzo SE. Prospects for time-of-flight PET using LSO scintillator. IEEE Trans. Nucl. Sci. 1999; 46:474–478.

Moszynski M, Kapusta M, Nassalski A, Szczesniak T, Wolski D, Eriksson L, Melcher CL. New prospects for time-of-flight PET with LSO scintillators. IEEE Trans. Nucl. Sci. 2006; 53:2484–2488.
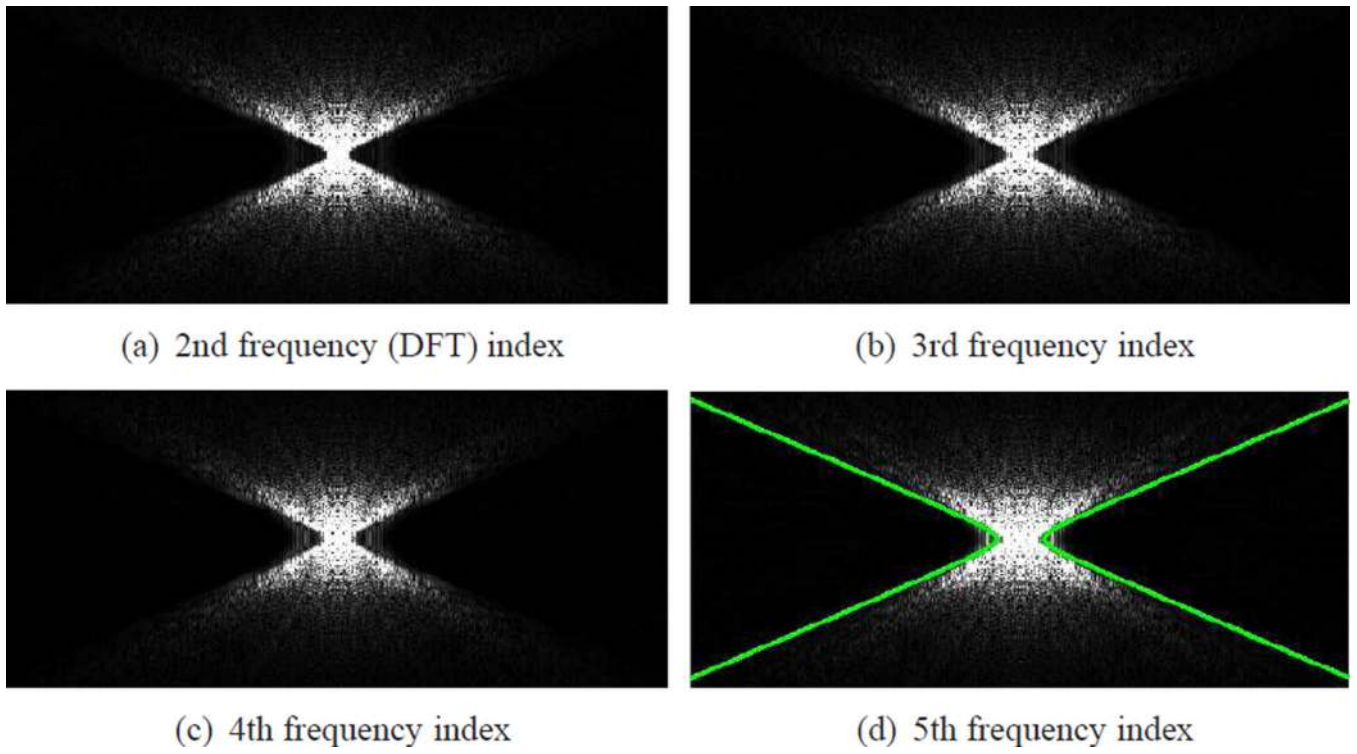
Mullani NA, Ficke DC, Hartz R, Markham J, Wong G. System design of fast PET scanner utilizing time-of-flight. IEEE Trans. Nucl. Sci. 1981; 28:104–107.

Parra LC, Barrett HH. List-mode likelihood - EM algorithm and noise estimation demonstrated on 2D-PET. IEEE Trans. Med. Imag. 1998; 17(2):228–235.

Rattey PA, Lindgren AG. Sampling the 2-D Radon transform. IEEE Tr. Acoust. Sp. Sig. Proc. 1981; 29(4):994–1002.

Siddon RL. Fast calculation of the exact radiological path for a three-dimensional CT array. Med. Phys. 1985; 12(2):252–255. [PubMed: 4000088]

Snyder DL, Politte DG. Image reconstruction from list-mode data in emission tomography system having time-of-flight measurements. IEEE Trans. Nucl. Sci. 1983; 20(3):1843–1849.

Snyder DL, Thomas LJ, Ter-Pogossian MM. A mathematical model for positron-emission tomography systems having time-of-flight measurements. IEEE Trans. Nucl. Sci. 1981; 28(3):3575–3583.

Surti S, Karp JS, Popescu LM, Daube-Witherspoon ME, Werner M. Invesigation of time-of-flight benefit for fully 3-D PET. IEEE Trans. Med. Imag. 2006; 25:529–538.

Surti S, Kuhn A, Werner ME, Perkins AE, Kolthammer J, Karp JS. Performance of Philips Gemini TF PET/CT scanner with special consideration for its time-of-flight imaging capabilities. J. Nuc. Med. 2007; 48:471–480.

Ter-Pogossian MM, Ficke DC, Yamamoto M, Hood JT. Super PETT I: A positron emission tomograph utilizing photon time-of-flight information. IEEE Trans. Med. Imag. 1982; 1(3):179–187.

Tomitani T. Image reconstruction and noise evaluation in photon time-of-flight-assisted positron emission tomography. IEEE Trans. Nucl. Sci. 1981; 28:4582–4589.

Vandenberghe S, Daube-Witherspoon ME, Lewitt RM, Karp JS. Fast reconstruction of 3D time-of-flight PET data by axial rebinning and transverse mashing. Phys. Med. Biol. 2006; 51:1603–1621. [PubMed: 16510966]

Watson CC. An evaluation of image noise variance for time-of-flight PET. IEEE Trans. Nucl. Sci. 2007; 54:1939–1947.
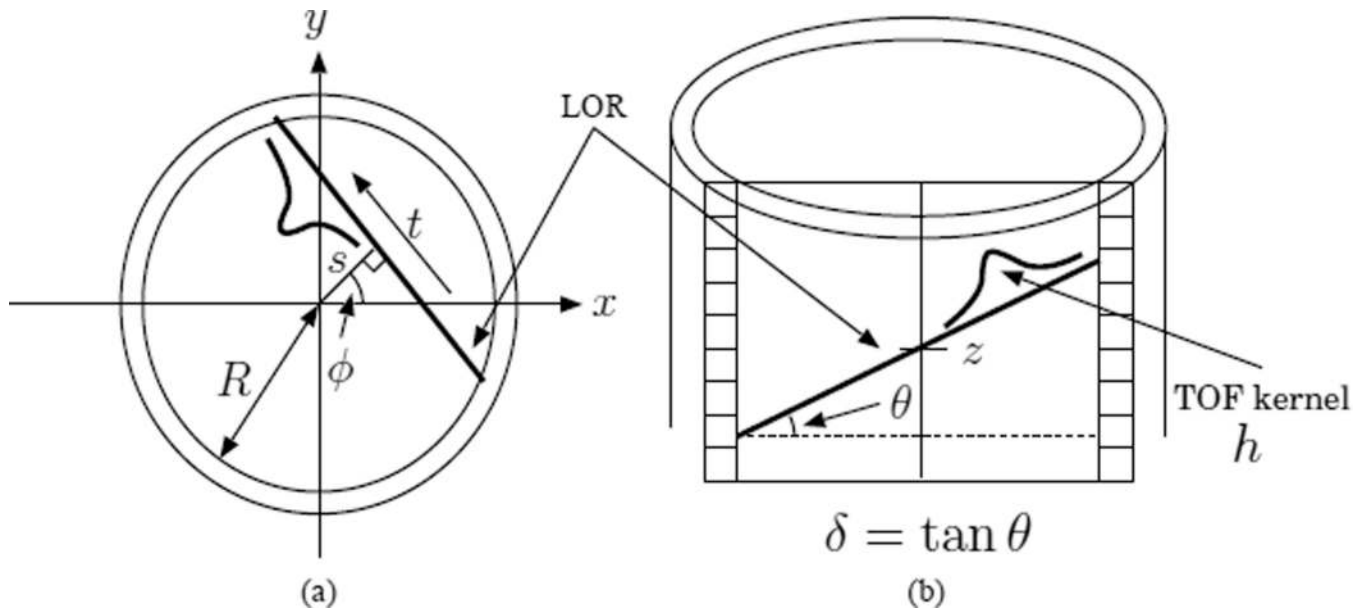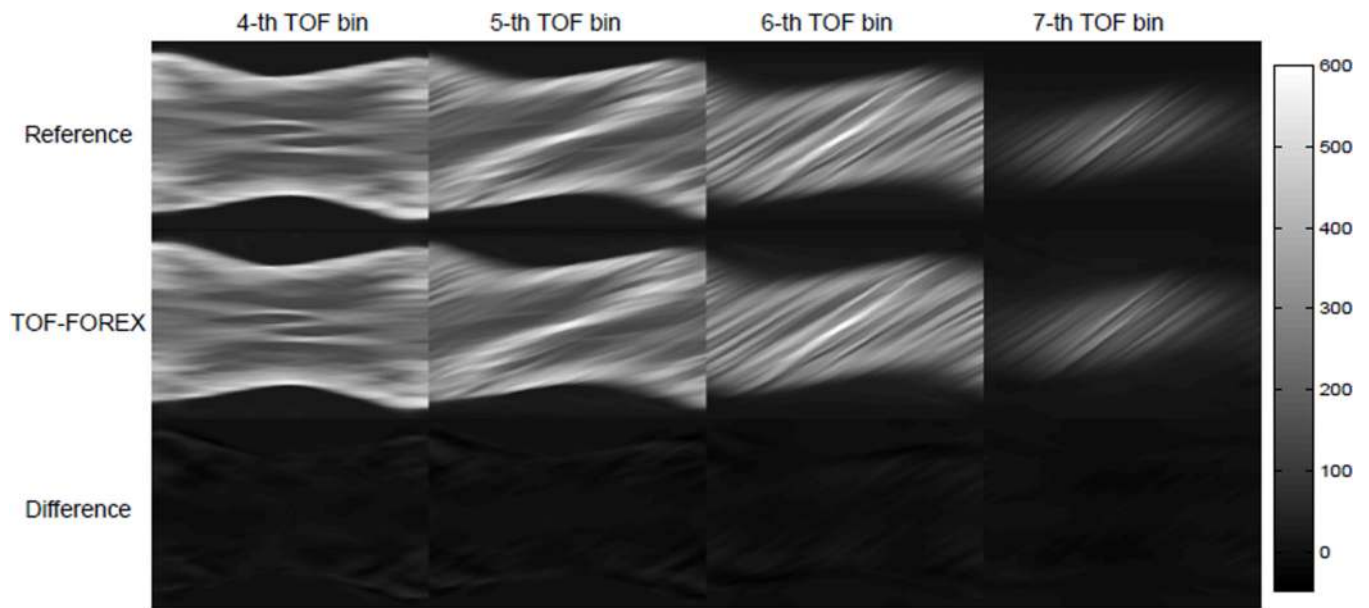
Figure 1.
(a) Top and (b) side view of a cylindrical 3D PET scanner. For each line of response (LOR), the object is multiplied by the TOF kernel h and integrated along the line to form the TOF data.

(a) center TOF bin

(b) 2nd TOF bin from the center bin

(c) After 1D Fourier transform in t at ω_t frequency index zero

(d) After 1D Fourier transform in t at ω_t frequency index 2

Figure 2.
2D TOF sinograms and their magnitudes after taking 1D Fourier transform in t; The horizontal axis is the sinogram angle $\varphi \in [0, 2\pi]$ and the vertical axis is the radial variable s.
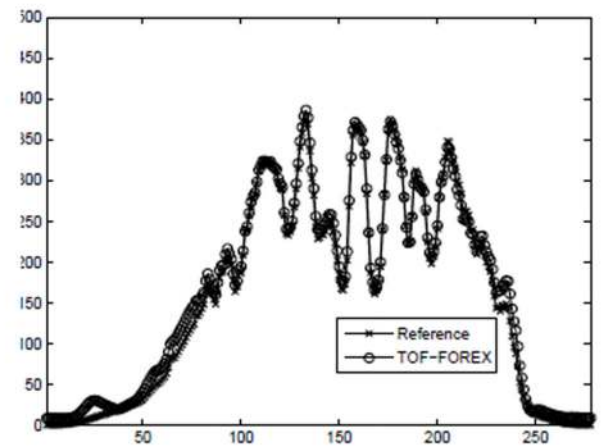
(a) 2nd frequency (DFT) index

(b) 3rd frequency index

(c) 4th frequency index

(d) 5th frequency index

Figure 3.
2D Fourier transform $\wp_{2D}(\omega_s, \omega_\varphi; \omega_t)$ of $\wp_{2D}(s, \varphi; \omega_t)$ in (12) for four different ω_t frequency indices. The horizontal axis represents ω_φ and the vertical axis ω_s. Also shown in (d) is the hyperbolic curve bounding the effective support of the bow-tie for TOF data in the 5th frequency bin.
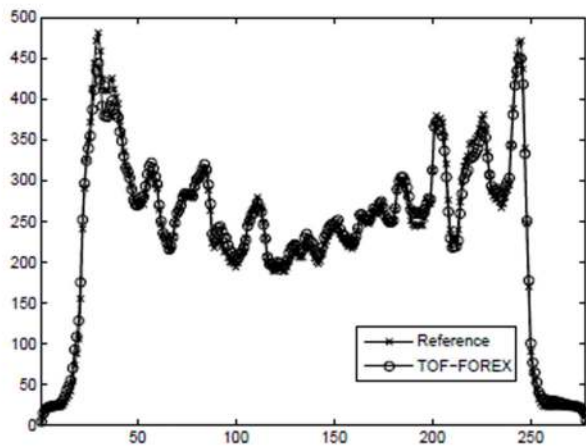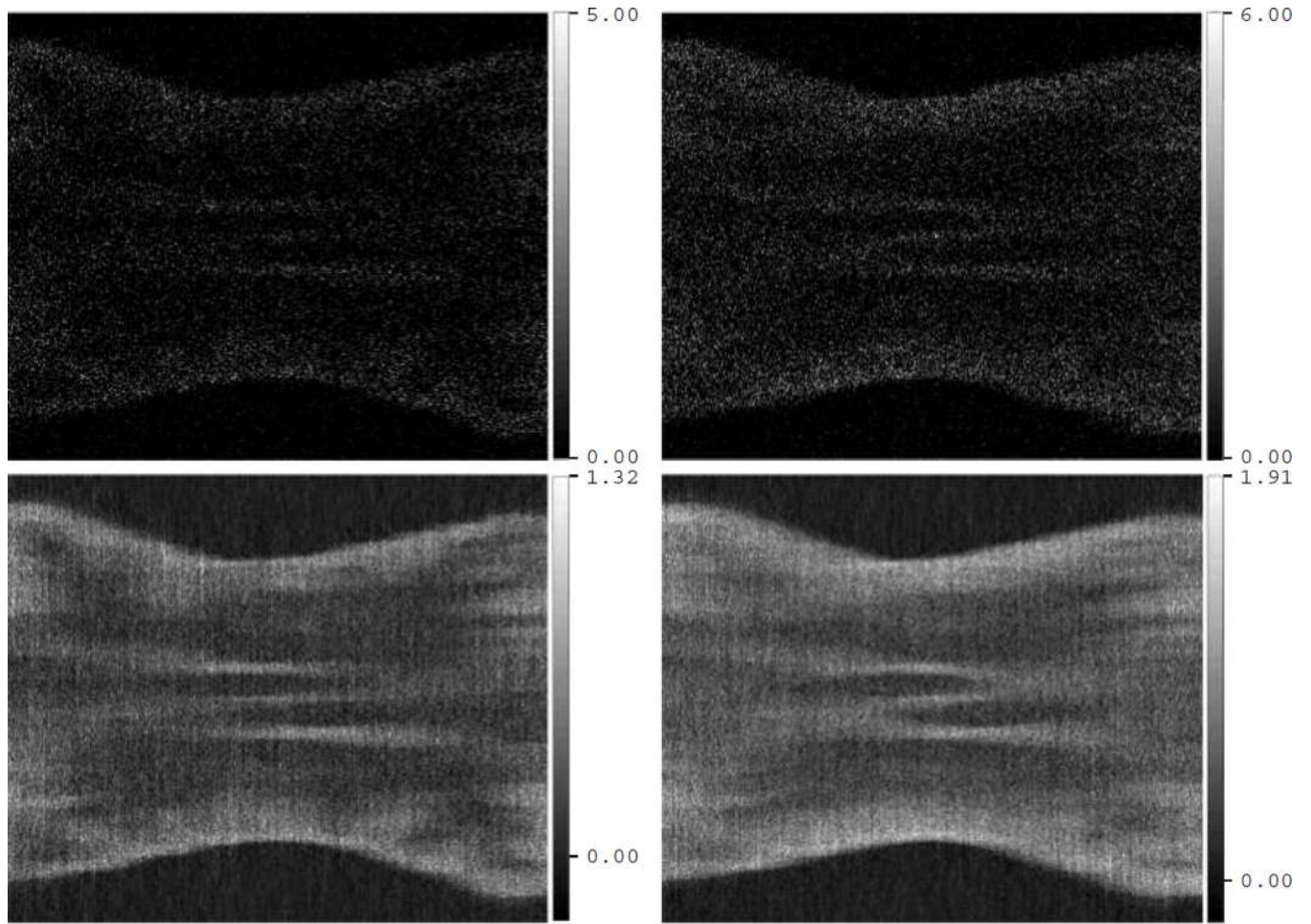
Figure 4.
Comparison of rebinned TOF sinograms with corresponding directly computed TOF sinograms (TOF timing resolution 500 ps); (a) Columns show TOF bin indices from 4 to 7; rows show the calculated direct sinogram (Reference), the rebinned sinogram (TOF-FOREX), and their difference (Difference); (b) radial profile through the sinograms for 4th TOF bin at 40-th angle; (c) radial profile through the sinograms for 7th TOF bin at 40-th angle
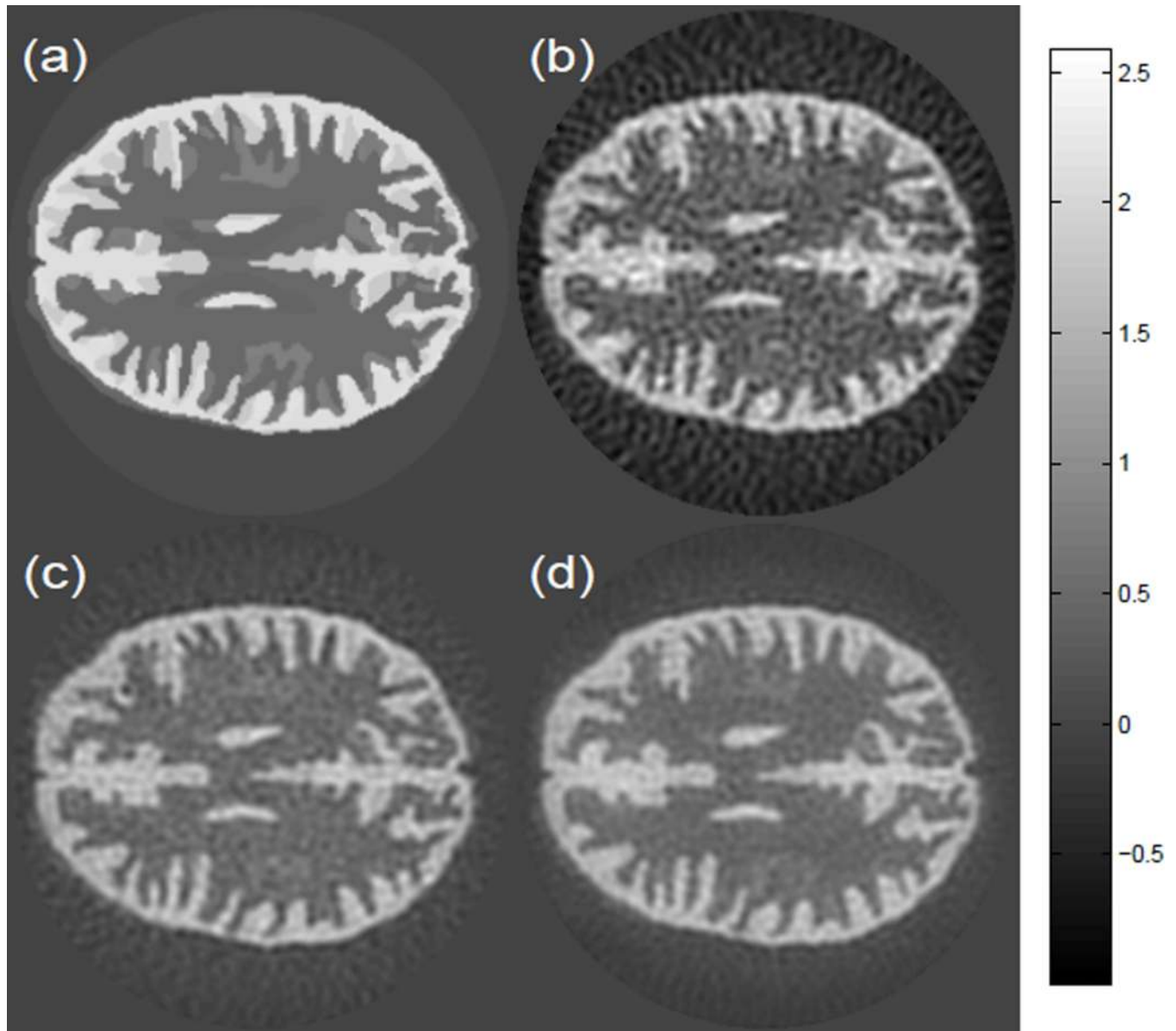
Author Manuscript

(a) TOF resolution: 500 ps

(b) TOF resolution: 250 ps

Figure 5.
Comparison of (top) noisy 2D direct sinogram with (bottom) noise reduction resulting from rebinning of oblique data into direct planes for (a) 500 ps, and (b) 250 ps resolution.

Figure 6.
3D reconstructions from 200 million counts for the central axial slice: (a) true image; (b) 3D non-TOF reconstruction: FOREX followed by direct 2D Fourier reconstruction; (c) 3D TOF reconstruction using TOF-FOREX followed by 2D TOF direct Fourier reconstruction with TOF timing resolutions of 500 ps: (d) as for (c) but with 250 ps resolution. The 3D Hoffman digital brain phantom was scaled to the size of 512mm×512mm×164mm to better demonstrate the effects of TOF information.

Table 1

Simulated 3D TOF cylindrical PET system parameters

Parameter	Value
Ring radius (mm)	421
Detectors per ring	672
Number of rings	41
Rays (LORs) per angle	336
Maximum ring difference (MRD)	27
Span	3
TOF resolution (ps)	250 (or 500)
Number of TOF bins	15 (or 7)
Image size	$256 \times 256 \times 81$
Transverse voxel size (mm)	2
Scanner axial FOV (mm)	164